Received 18 July 2022; revised 9 August 2022; accepted 15 August 2022. Date of publication 25 August 2022; date of current version 15 September 2022.

Digital Object Identifier 10.1109/OJAP.2022.3201617

A New Arraying Technique for Band-Switchable and Polarization-Reconfigurable Antenna Arrays With Wide Bandwidth

J. HUANG [1] (Member, IEEE), M. SHIRAZI [2] (Member, IEEE), AND X. GONG [3] (Senior Member, IEEE)

[1]Qorvo Inc., Apopka, FL 32703, USA

[2]Qualcomm Inc., San Diego, CA 92121, USA

[3]Antenna, RF and Microwave Integrated System Laboratory, University of Central Florida, Orlando, FL 32816, USA

CORRESPONDING AUTHOR: J. HUANG (e-mail: jensenhuang0@gmail.com)

This work was supported by the Defense Advanced Research Projects Agency (DARPA) Arrays at Commercial Timescale (ACT) Program under Grant HR0011-140100003.

ABSTRACT Modern antenna arrays desire antenna apertures which can support a wide frequency range and reconfigurable polarization states. It is challenging to realize such antenna apertures with high isolation among different antenna elements when they are closely packed, particularly for wide-band (>2:1 frequency ratio) operations. In this paper, we demonstrated switchable-band antenna arrays which can be reconfigured from S to C band with an instantaneous bandwidth close to 2:1. The major novelty in this antenna array is that a new arraying technique is adopted to reduce the number of feeding ports by 50%. As a result, the isolation among antenna elements can be significantly improved, thereby increasing the overall radiation efficiency. It should be noted that vertical, horizontal and circular polarizations are supported by this antenna array when all ports are provided with appropriate phases. Herein two arrays are demonstrated. Array I is based on a fractal-shaped slot-ring structure. Each antenna element is fed by a microstrip along the diagonal direction. The common antenna aperture can be reconfigured to operate at 2.5-4.0 GHz or 4.2-7.2 GH, using PIN diode switches. Array II is extended from Array I but with an Artificial Magnetic Conductor (AMC) ground to enhance the instantaneous bandwidth to 2:1. The length of the microstrip feeding lines are reduced to enable modular design. In addition, PIN diode switches are embedded in the feeding lines to further improve the isolation and radiation efficiency. The return losses, port isolations, radiation patterns, gains, radiation efficiencies and IIP_3 are simulated and measured.

INDEX TERMS Antenna arrays, reconfigurable antennas, switchable antennas, ultra wideband antennas.

I. INTRODUCTION

IN VARIOUS wireless applications such as communication systems or radars, a wide frequency coverage is often desired. This can be achieved using wide-band [1], [2], [3], [4], [5], [6], [7], [8] and multi-band [9], [10], [11], [12], [13], [14], [15], [16] antenna arrays. Among them, dual polarization states were demonstrated in [5], [6], [7], [8] and [13], [14], [15], [16].

Typically, a dual-polarized antenna requires two feeding ports which excite the orthogonal polarization states, respectively [17], [18], [19], [20], [21]. For a large antenna array, the large number of ports leads to energy loss due to the limited isolation between the feeding lines within the same antenna element or between neighboring elements. It is observed that there is a general tradeoff between the isolation level and instantaneous fractional bandwidth (FBW) when a dual-polarized antenna element is concerned [17], [18], [19], [20], [21].

For a narrow-band tunable slot-ring antenna [22], the isolation between the vertical (V) and horizontal (H) feeding ports degrades from 34 to 16 dB when the frequency is tuned from 0.93 (0.5% FBW) to 1.6 GHz (5% FBW). By incorporating fractal shapes into the square slot-ring, FBWs up to 66.7% (2:1 frequency ratio) were demonstrated [23], [24]. This wide FBW led to up to 5/4 dB isolation between the two orthogonal ports at *S*/*C* band, respectively [24]. The

This work is licensed under a Creative Commons Attribution 4.0 License. For more information, see https://creativecommons.org/licenses/by/4.0/

radiation efficiencies are reduced from 80%(*S* band)/90%(*C* band) to approximately 50% at both bands, due to this limited isolation.

A new arraying technique is developed here by feeding each antenna element along the diagonal direction. In this configuration, only one feed is required for each antenna element. The different polarization states can be achieved by feeding the antenna ports with appropriate phases which will be articulated in Section II. There are two main advantages: (1) the number of antenna ports is reduced by 50%; (2) the isolation issue between the two orthogonal polarization states inside the same antenna element is completely mitigated.

This arraying concept is similar to [25] but with distinctions whereas a circularly polarized (CP) antenna array be formed using linearly polarized (LP) antenna elements through sequential rotation. It is noted that neither the operation frequency nor the polarization state can be changed in [25]. In another development [26], antenna elements are linearly polarized along ±45° directions. However, the polarization state of the entire array is also along ±45° directions. The array in [26] can reconfigure the radiation pattern from broadside to monopulse with the assistance from a complex switching network.

In this paper, we will present two arrays which can realize vertical (V), horizontal (H), and circular polarization states at the array level while each element is polarized along the diagonal direction. It should be noted that both Arrays I&II are band-switchable antenna arrays with wide instantaneous FBW. The works presented here are part of Huang's doctoral dissertation [27].

In Array I, a ground plane using copper is placed $\lambda_0/4$ (@4.7 GHz) below the radiating aperture to realize single-sided radiation. However, due to the wide bandwidth (a total of 4:1 frequency ratio) of this array, the realized gain cannot stay flat across the entire frequency range. Therefore, Artificial Magnetic Conductor (AMC), a form of Electromagnetic bandgap (EBG) structures [28], [29], [30], [31], [32], is used in Array II to replace the copper ground plane in Array I. In earlier works [33], [34], [35], bandwidths up to 10:1 were demonstrated for antennas using AMC. On the other hand, AMC can be used to support dual-band antenna designs [36], [37], [38], [39].

There are two extra efforts in Array II designs. First, the microstrip feeding lines are shrunk to the perimeter of the slot ring, which is necessary to extend the array to a larger size (modular design). Second, to further improve the isolation between the *S* and *C* band operation states, a few PIN diode switches are embedded in the feeding lines at both bands, which lead to higher radiation efficiencies and realized gains.

The design of Array I using the proposed arraying technique is presented in Section II. The fabrication and measurement results of Array I are discussed in Section III. The design of Array II with AMC is explained in Section IV while its fabrication and experimental results are shown in Section V. The comparison of both arrays with the State of the Art is summarized in Section VI.

II. ARRAY I DESIGN

A. ARRAY I RADIATION APERTURE DESCRIPTION

As shown in Fig. 1, Array I is composed of several layers. The top layer is a substrate with the fractal-shaped slot rings on the bottom side and microstrip feeding lines on the top. At $\lambda_g/4$ (@5 GHz) below the top layer is a copper plate. Multiple micro-coaxial lines are vertically connected to the microstrip lines and pass through small holes drilled inside the copper plate (Fig. 1(d)). The center pins of the micro-coaxial lines pass through the substrate and are soldered to the microstrip lines while the outer conductors of the micro-coaxial lines are soldered to the slot rings.

Array I is composed of 2×2 *S*-band antenna elements as shown in Fig. 1(a). Each *S*-band element is fed by two perpendicular microstrip lines connected at the center of the antenna. As shown in Fig. 1(b), 8 PIN diode switches are embedded inside the radiation aperture. When all of them are turned off, the thin meandering lines connecting the switches are not shorted, therefore the slots in the entire *S*-band element can form multiple resonances at *S* band. When all the PIN diode switches are turned on, the *S*-band element is divided into 4 smaller slot-rings. One smaller slot-ring is illustrated in Fig. 1(c) and can create multiple resonances at *C* band. The *C*-band element is fed by a microstrip line along the diagonal direction. It should be noted that this switchable-band design can maintain half-length array element spacing across a 4:1 frequency bandwidth [24].

All PIN diode switches share the same biasing voltages since they are turned on and off at the same time. As shown in Fig. 1(c), the metal area connected to the positive (negative) terminal of the diodes is labeled as Area I (II). Area II is connected to the outer conductors of the micro-coaxial lines therefore can be considered as ground. The DC voltage of Area I is provided by an enameled wire which is soldered at the conner of the array elements. Since the outer conductors of the micro-coaxial lines for the *C*-band elements are also connected to Area I, a circular ring is cut around the *C*-band element feeding line in order to provide DC voltage isolation. The gap size in the circular ring and location of the bias wire are verified in ANSYS High Frequency Structure Simulator (HFSS) to present negligible effects on the antenna performance.

B. ARRAYING TECHNIQUE

A square slot-ring antenna can be excited by microstrip lines at different locations as shown in Fig. 2(a). When the microstrip lines are placed at the center of the vertical slots, H polarizations can be excited. Antennas I and II represent two different scenarios considering the location of the coaxial line. Both Antennas III and IV can provide LP along the diagonal direction. All four feeding methods provide similar frequency bandwidths as shown in Fig. 2(b).

Fig. 3 illustrates the operation principle of this new arraying technique. In Fig. 3(a), when a_1-d_1 are provided with the phases shown in the figure, the horizontal components of the radiated fields cancel while the vertical components

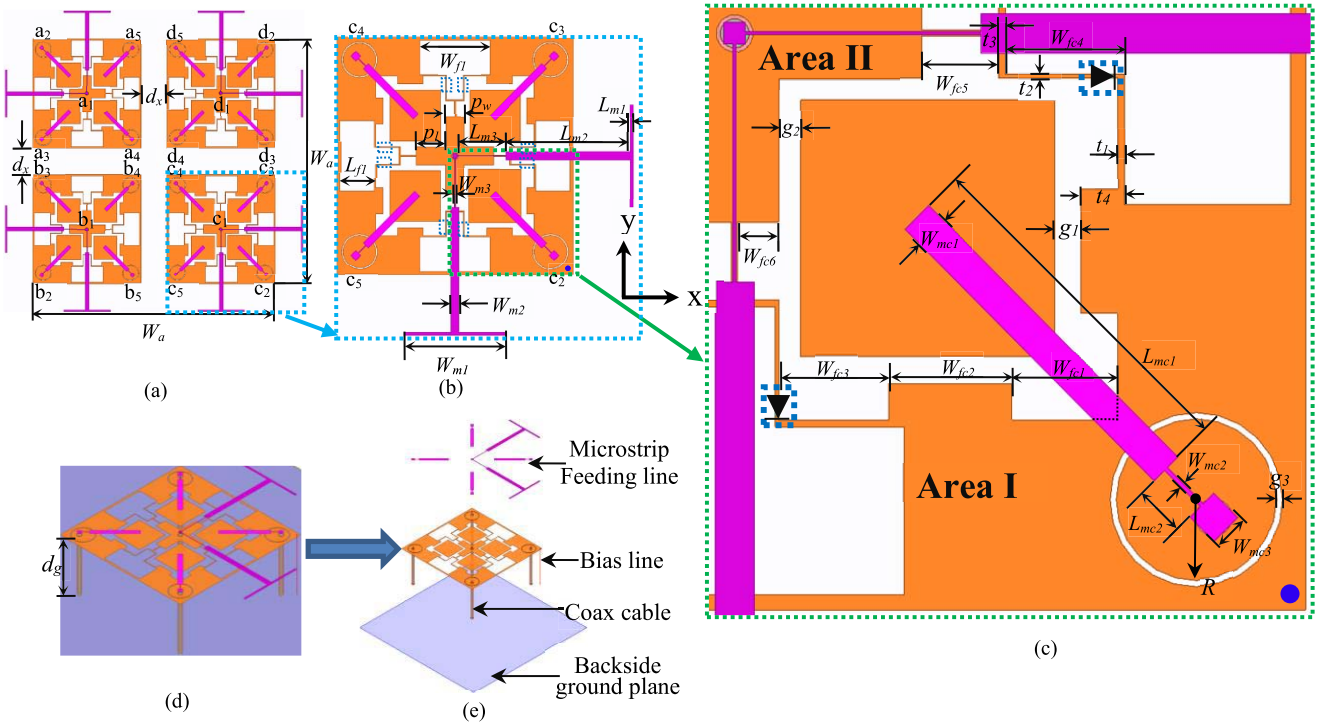

FIGURE 1. (a) Schematic of Array I. (b) Array I dual-band element. (c) Array I *C*-band element. (d) The side view and (e) exploded view. $d_x = 9$, $W_a = 83$, $W_{m1} = 16$, $W_{m2} = 1.27$, $W_{m3} = 0.1$, $L_{m1} = 0.5$, $L_{m2} = 20.3$, $L_{m3} = 7.7$, $p_w = 2.86$, $p_l = 4.635$, $L_{f1} = 5.4$, $W_{f1} = 11$, $t_1 = 0.22$, $t_2 = 0.11$, $t_3 = 0.235$, $t_4 = 1.4$, $W_{fc1} = 3.45$, $W_{fc2} = 4$, $W_{fc3} = 3.57$, $W_{fc4} = 3.85$, $W_{fc5} = 2.5$, $W_{fc6} = 1.33$, $W_{mc1} = 1$, $W_{mc2} = 0.25$, $W_{mc3} = 1$, $L_{mc1} = 11.6$, $L_{mc2} = 1.65$, $g_1 = 1.05$, $g_2 = 0.88$, $g_3 = 0.2$, $R = 2.6$ and $d_g = 16$. All dimensions are in mm.

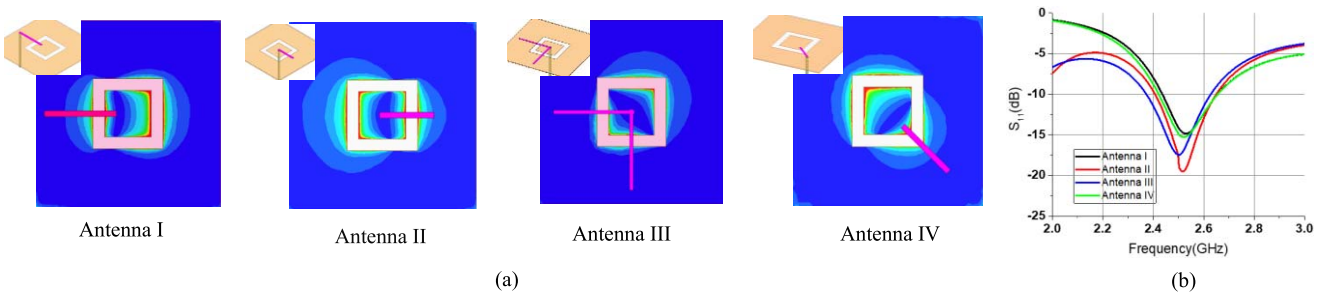

FIGURE 2. (a) Comparison of different feeding methods for a square slot-ring. (a) E-field distributions at 2.5GHz and (b) S_{11} of Antennas I-IV.

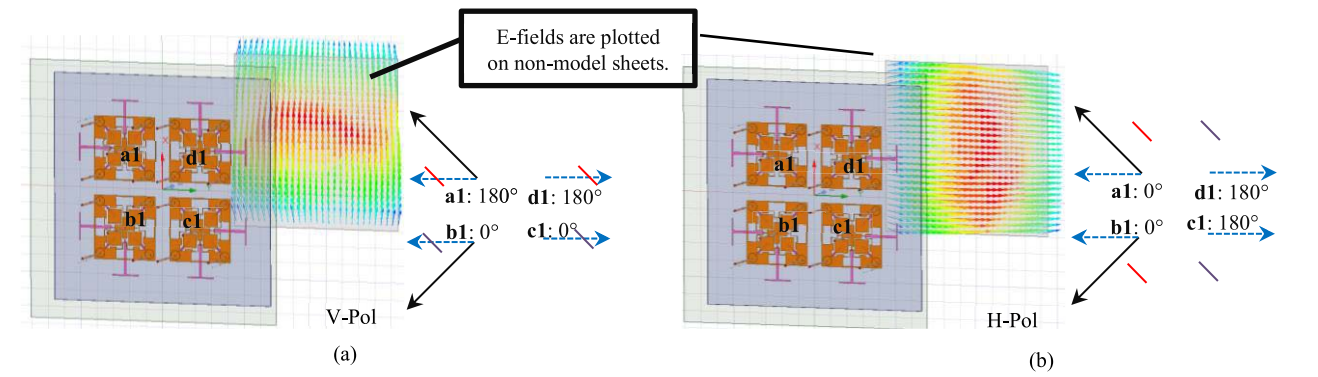

FIGURE 3. New arraying technique to realize (a) vertical and (b) horizontal polarizations from antenna elements fed along diagonal directions.

add up. H polarization can be realized similarly as shown in Fig. 3(b). This arraying technique was first presented in [40] by the same authors. However, the design in [40] requires a physical rotation of the antenna aperture when the operation frequency band is switched from *S*(*C*) to *C*(*S*) band. In the two designs here, no physical movement of the

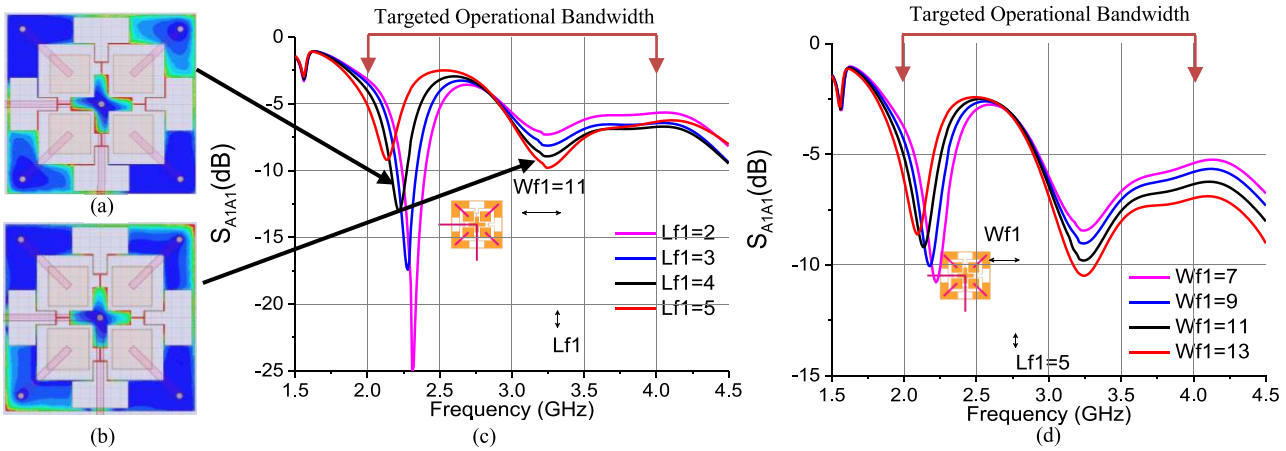

FIGURE 4. E-field of the *S*-band element at (a) 2.1 and (b) 3.2 GHz. S_{11} of the *S*-band element with different (c) W_{f1} and (d) L_{f1}. (All dimensions are in mm).

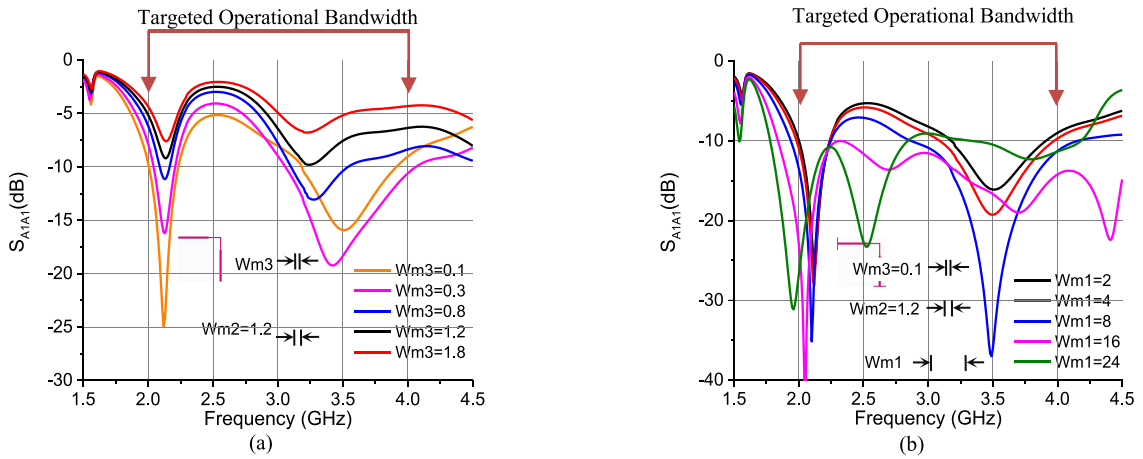

FIGURE 5. S_{11} of the *S*-band element with different (a) W_{m3} and (b) W_{m1}. (All dimensions are in mm.)

antenna aperture is needed when either operation frequency or polarization state is reconfigured.

C. ARRAY I DESIGN PROCEDURE

The fractal-shaped slot-ring antennas in [23], [24] can achieve up to 66.7% FBW at both *S* and *C* bands. However, the shape of the *S*-band element resembles that of the *C*-band element but with a 45° rotation. This leads to the aforementioned issue in [40]. **Therefore, new fractal shape designs are necessary to accommodate the new arraying technique.**

The array element design starts from the *S*-band slot ring. A first-order fractal shape is incorporated into a square slot-ring as shown in Fig. 4. The fractal design introduces a second resonance in addition to the fundamental mode at approximately 2.4 GHz. This fundamental resonance decreases in frequency when the slot size $L_{f1}\times W_{f1}$ increases [41], [42]. The second resonance becomes stronger around 3.3 GHz when L_f is swept from 2 to 5 mm for W_f of 11 mm as shown in Fig. 4(c). As suggested by the electric field distribution in Figs. 4(a) and 4(b), the polarization of this antenna element is along 45° direction similar to the Antenna III (Fig. 2(a)). Fig. 4(d) studies the effect of W_{f1} when L_{f1} is fixed at 5 mm. It is observed that W_{f1} exhibits a much less impact on S_{11} of the antenna. W_{f1} of 11 mm and L_{f1} of 5 mm yield the best antenna matching for now.

The *S*-band antenna impedance matching can be further improved by using dual-branch stepped impedance microstrip lines as shown in Fig. 5. To minimize the design variables, the length of each branch is set to 28 mm while W_{m2} is fixed at 1.2 mm. In Fig. 5(a), it is observed that the larger impedance contrast renders better impedance matching. W_{m3} of 0.1 mm yields the best result. However, in the middle of the targeted operational frequency band (2-4 GHz), the S_{11} is above -10 dB in the middle of the band. Finally, W_{m1} is studied in Fig. 5(b) and it was found that W_{m1} of 16 mm can provide <-10 dB S_{11} within the entire S band.

Next, the *C*-band elements are added to the optimized *S*-band element as shown in Fig. 6(c). The *C*-band element is also a first-order fractal-shaped slot-ring but with slightly

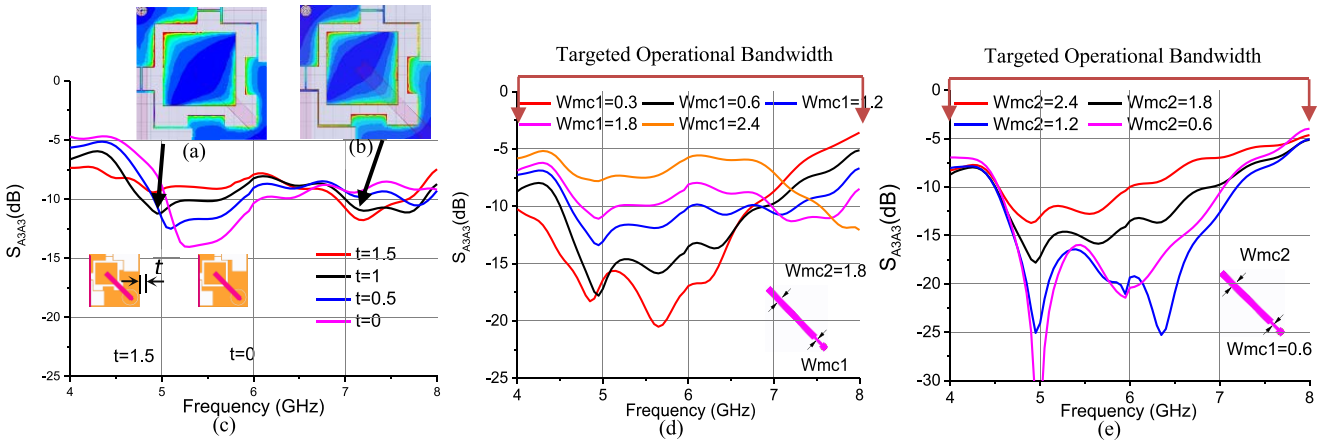

FIGURE 6. E-field of the *C*-band element at (a) 5 and (b) 7.2GHz. S_{33} of the *C*-band element vs. (c) *t*, (d) W_{mc1} and (e) W_{mc2}. (All dimensions are in mm.)

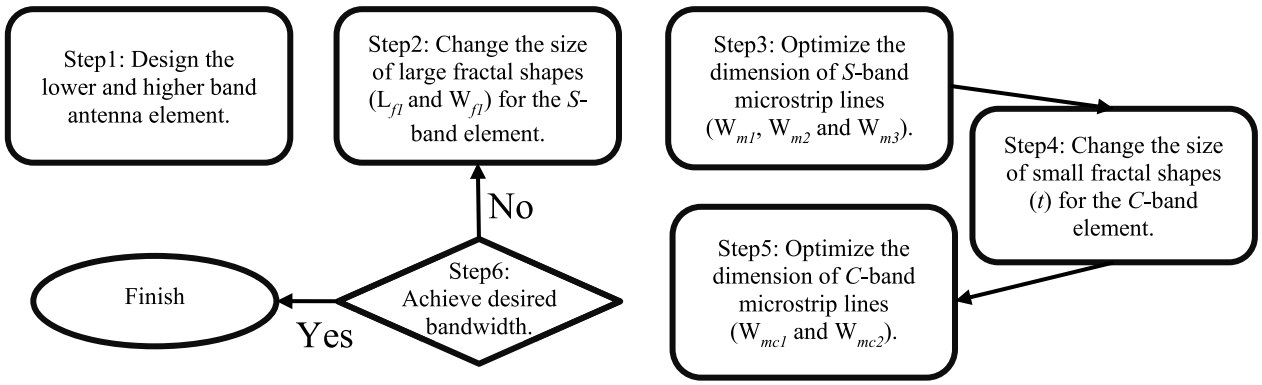

FIGURE 7. The design flow chart for Array I.

different arrangement. In Fig. 6(c), *t* of 1 mm can equally excite two resonance modes at *C* band. The E fields shown in Figs. 6(a) and 6(b) resembles that of Antenna IV (Fig. 2a), showing a LP along -45° direction.

In Array I element design, we used two different feeding line along the diagonal directions to avoid the overlap between them. The *C*-band feeding line is also a stepped-impedance microstrip line. Figs. 6(d) and 6(e) study the effect of W_{mc1} and W_{mc2}, respectively. The combination of W_{mc1} of 0.6 mm and W_{mc2} of 1.2 mm can provide $S_{33} < -10$ dB from 4.5 to 7.2 GHz. This is the best result we can achieve in Array I though the target is 4-8 GHz.

The design procedure is illustrated in Fig. 7. It is noted that the optimization of *C*-band elements slightly perturbs the matching of the *S*-band element. A second iteration might be necessary to obtain good impedance matching in both bands.

III. ARRAY I FABRICATION AND MEASUREMENT

A. FABRICATION

The antenna substrate is 31-mil-thick Rogers RT/Duroid 5880 ($\varepsilon_r = 2.2$ and $\tan\delta = 0.0009$). The fractal-shaped slot-ring antenna array and its feeding lines are etched on both sides of the substrate as shown in Figs. 8(a) and 8(b). The diameters of the inner and outer conductors of the micro-coaxial line are 0.58 and 1.68 mm, respectively. 32 PIN diode switches (Skyworks DSM-8100) are mounted using silver paste (SPI 05002-AB from Structure Probe, Inc.). The equivalent circuit and power consumption of these PIN diode switches were investigated by the same authors [43].

According to Fig. 1, the holes in the ground plane should be barely larger than the out conductor of the micro-coaxial line to avoid backside radiation. However, this makes it difficult to replace a failing PIN diode switch since the ground plane cannot be removed without de-soldering all coaxial lines. A dual-layer ground plane design is illustrated in Figs. 8(c) and 8(d). The holes in Ground Plane I are large enough to allow the connectors to pass through. Meanwhile the holes in Ground Plane II are still very small. However, additional slots are carved in Ground Plane II to expose all the switches. When a repair is deemed necessary, Ground Plane I can be removed, and the de-soldering of PIN diode switches can be done though the slots.

As shown in Fig. 8(e), the micro-coaxial lines pass through the holes in Ground Plane II and then are soldered to the antenna substrate. A zoom-in view of this connection for a *C*-band element is shown in Fig. 8(f). Next, Ground Plane I is mounted. 3-D printed plastic support structures are used to assembler the antenna array as shown in Figs. 8(g)-(i). It

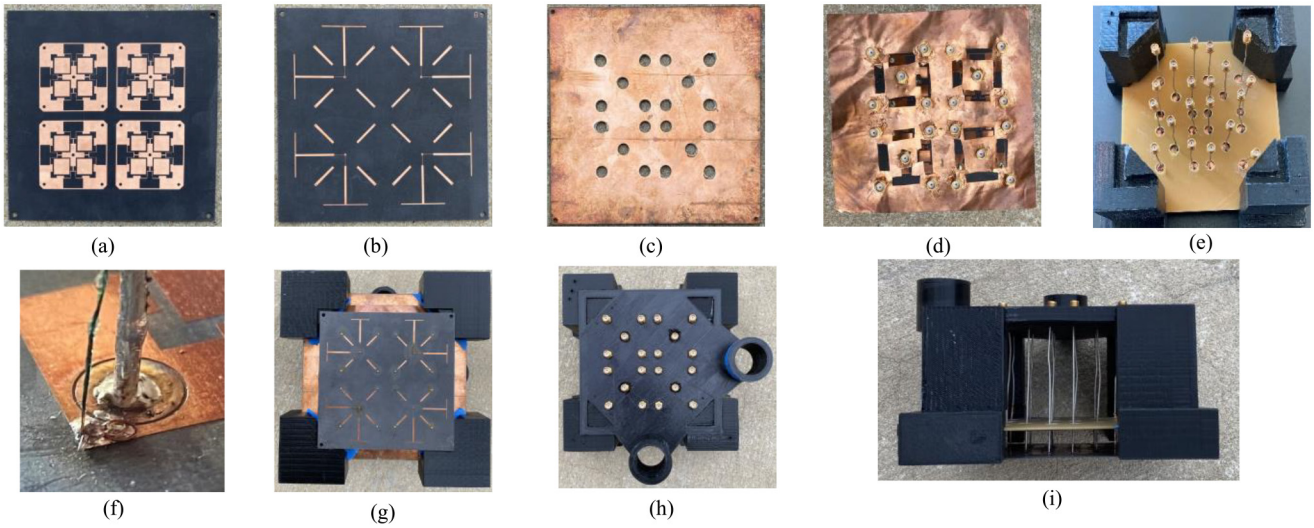

FIGURE 8. Array I (a) radiation aperture and (b) feeding lines. (c) Ground Plane I. (d) Ground Plane II. (e) Coax feeding. (f) C-band element feeding and bias wire. (g) Top, (h) bottom and (i) side view of assembled antenna array.

should be noted that the length of the micro-coaxial cables can be significantly reduced (all the way to the ground plane) without unfavorably affecting the antenna performance.

B. RETURN LOSSES AND MUTUAL COUPLING

The return losses of all four *S*-band ports are presented in Fig. 9(a). The actual operational bandwidth (S11<-10 dB) is 2.5-4.0 GHz. The measured responses of the four S-band ports are consistent with each other and agree with the simulations. In Fig. 9(b), the return losses of all four C-band ports (within the top left *S*-band element) are presented. The actual operational bandwidth is 4.2-7.2 GHz.

Since this array can provide beam-steering capability, it is important to check the mutual coupling among different ports. First, the active S parameters at *S*(*C*) band are shown to be close to S parameters in Fig. 9(c) (Fig. 9(d)). This implies that the mutual coupling does not significantly impact the impedance matching of each antenna element inside the entire array. In addition, the mutual coupling for several different cases is illustrated in Fig. 9(e)-(f) and Fig. 10, respectively. Fig. 9(e) (Fig. 9(f)) presents the coupling from an *S*-band port (all *C*-band ports) to the four *C*-band ports (the *S*-band port) within the same aperture at *S*-band (*C*-band) operation state. The measured coupling level is less than -12 dB at both bands of operation. The mutual coupling between any two of the four *S*-band ports (*C*-band ports in the same *S*-band aperture) is shown in Fig. 10(a) (Fig. 10(b)-(c)) and is lower than -25 dB (-15 dB) in most of the frequency range. Regarding the mutual coupling between the *C*-band ports inside different *S*-band elements, only a_4, b_4, c_4, and d_4 are studied and presented in Fig. 10d(d) since they are close to each other. This mutual coupling level is below -16 dB. For the brevity of presentation, the mutual coupling between *C*-band ports in other cases are not shown here and also found to be much smaller in HFSS simulations. It is noted that the mutual coupling shown in Fig. 10(a)-(d) does not impact radiation efficiency since they represent in-band coupling.

The coupling between ports of different bands does contribute to losses. In Fig. 9(e)-(f), such coupling in the same *S*-band element is shown. This coupling between ports of different bands within different *S*-band elements is also simulated and measured in Fig. 10(e)-(f). As expected, these coupling levels are very low (<-20 dB) in both operation bands.

C. RADIATION PATTERN

The radiation patterns of *S* and *C* band arrays for the vertical polarization are simulated and measured. In a digital array, the amplitude and phases at each port can be arbitrary. However, to demonstrate the radiation patterns herein, customized feeding networks are used to provide the 180-degree phase at some ports as illustrated in Fig. 11.

The co-polarization (Co-pol.) and cross-polarization (X-pol.) patterns in both E and H planes at four different frequencies in two bands are illustrated in Fig. 12. The measured patterns agree well with HFSS simulations. At the *C*-band state, the measured X-pol. levels are 23 dB below the Co-pol. levels at the boresight direction. At *S*-band, the simulated X-pol. level is less than -40 dB. However, the measured X-pol. level is <-10 dB. This might be due to the small ground plane size. Any misalignment between the ground plane and slot-ring aperture can cause increase X-pol levels, particularly at *S* band. In HFSS simulations, this misalignment does not exist.

D. REALIZED GAIN

The realized gain is measured using an Agilent network analyzer (N5230A) and the anechoic chamber at UCF. The reference plane is calibrated to the micro-coaxial connectors.

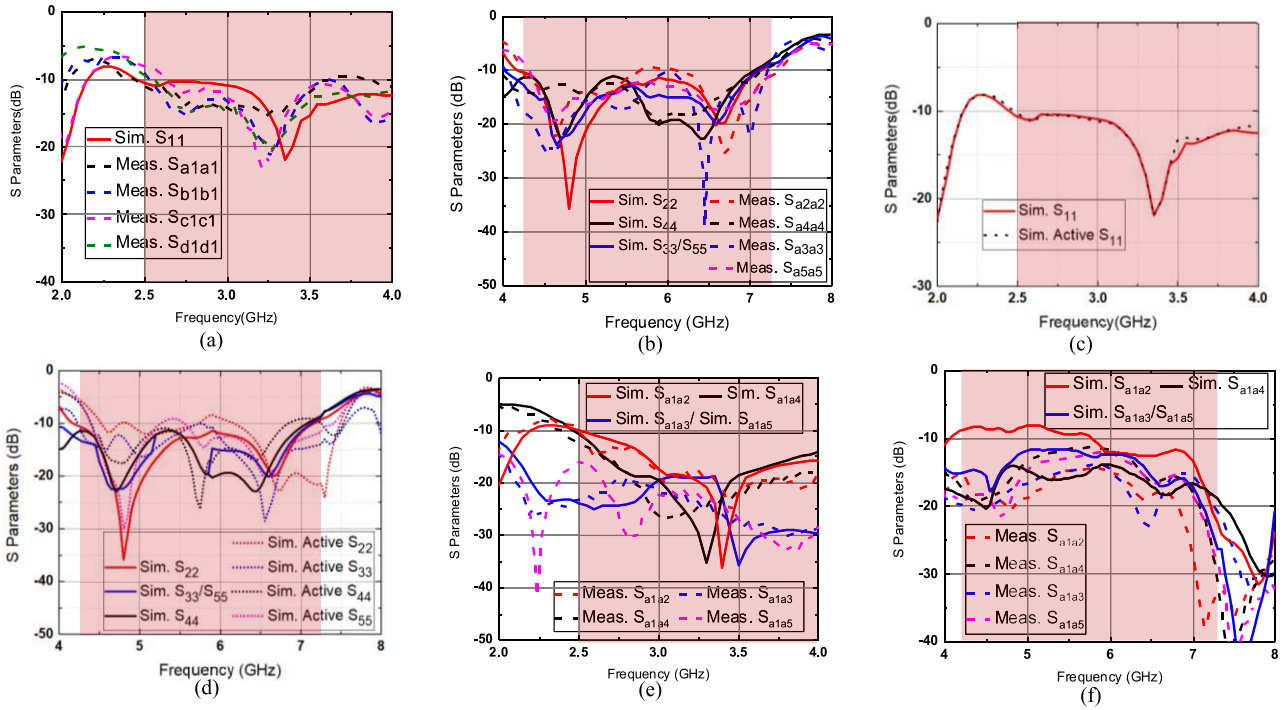

FIGURE 9. Simulated and measured (a) $S_{a1a1}/S_{b1b1}/S_{c1c1}/S_{d1d1}$ at the *S*-band state and (b) $S_{a2a2}/S_{a3a3}/S_{a4a4}/S_{a5a5}$ at the *C*-band state; simulated (c) S_{11} and active S_{11} at the *S*-band state, (d) $S_{22}/S_{33}/S_{44}/S_{55}$ and active $S_{22}/S_{33}/S_{44}/S_{55}$ at the *C*-band state; simulated and measured S_{a1a2}, S_{a1a3}, S_{a1a4} and S_{a1a5} at the (e) *S*-band state and (f) *C*-band state.

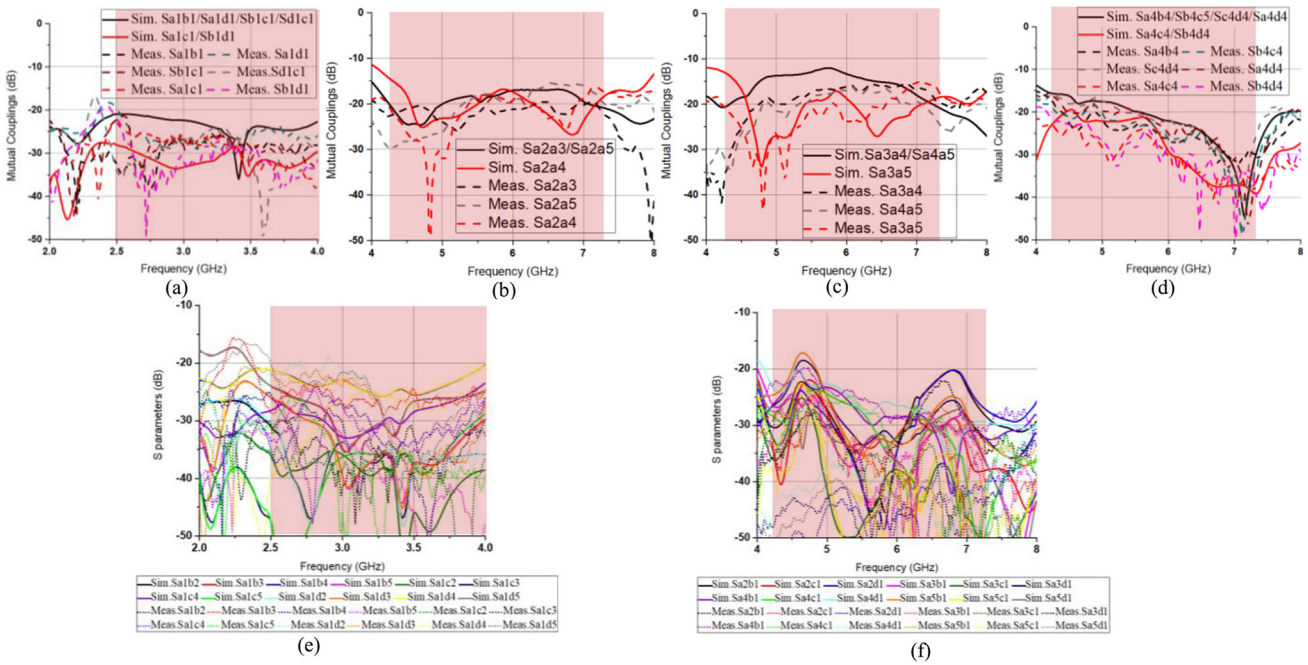

FIGURE 10. Simulated and measured (a) $S_{a1b1}/S_{a1c1}/S_{a1d1}/S_{b1c1}/S_{b1d1}/S_{c1d1}$ at the *S*-band state; (b) $S_{a2a3}/S_{a2a4}/S_{a2a5}$; (c) $S_{a3a4}/S_{a4a5}/S_{a3a5}$; (d) $S_{a4b4}/S_{a4c4}/S_{a4d4}/S_{b4c4}/S_{b4d4}/S_{c4d4}$ at the *C*-band state. (e) $S_{a1b2}/S_{a1b3}/S_{a1b4}/S_{a1b5}/S_{a1c2}/S_{a1c3}/S_{a1c4}/S_{a1c5}/S_{a1d2}/S_{a1d3}/S_{a1d4}/S_{a1d5}$ at the *S*-band state; (f) $S_{a2b1}/S_{a2c1}/S_{a2d1}/S_{a3b1}/S_{a3c1}/S_{a3d1}/S_{a4b1}/S_{a4c1}/S_{a4d1}/S_{a5b1}/S_{a5c1}/S_{a5d1}$ at the *C*-band state. (The actual bandwidth is covered under the red shape.)

As shown in Fig. 13(a)-(b), the measured realized gain is above 5.7 (11.5) dBi in *S*(*C*) band. The overall efficiency of the *S*(*C*) band array is simulated in HFSS and shown to be 55-80% (60-82%) at the *S*(*C*)-band state. In HFSS simulations, losses from metal, dielectric material and switches are included.

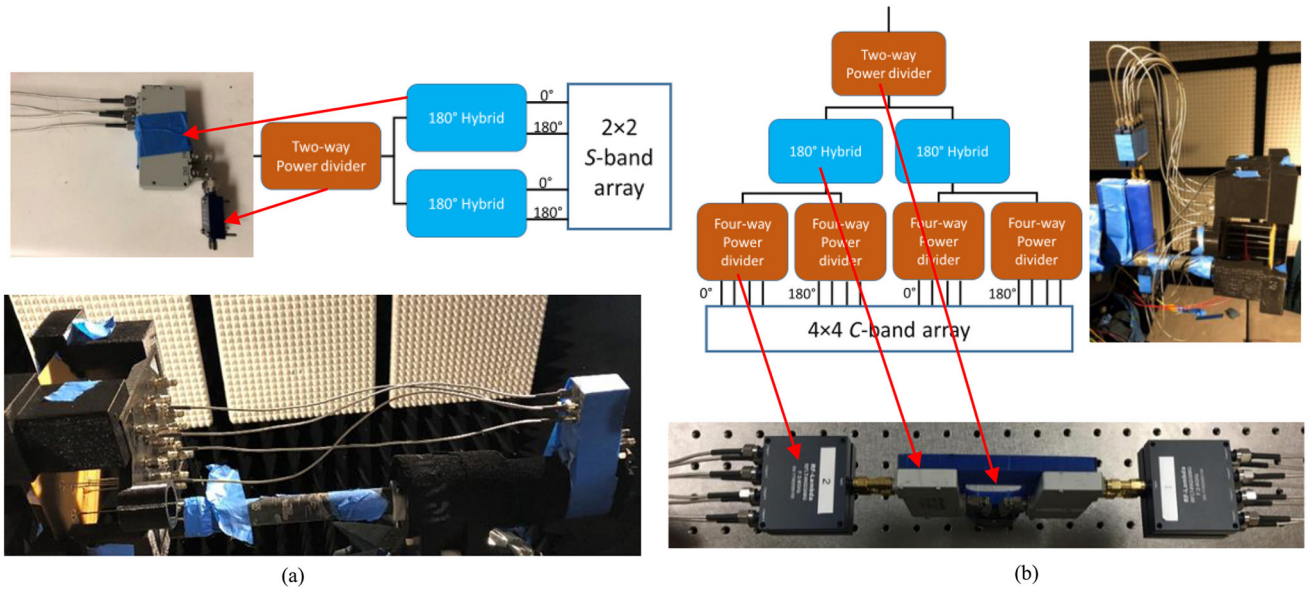

FIGURE 11. Feeding network for (a) S-band and (b) C-band arrays. Two-way power divider (RFLT2W2G08G). 180° hybrids (RFHB02G08GPI). Four-way power dividers (RFLT4W2G08G). All of them are purchased from RF-Lambda.

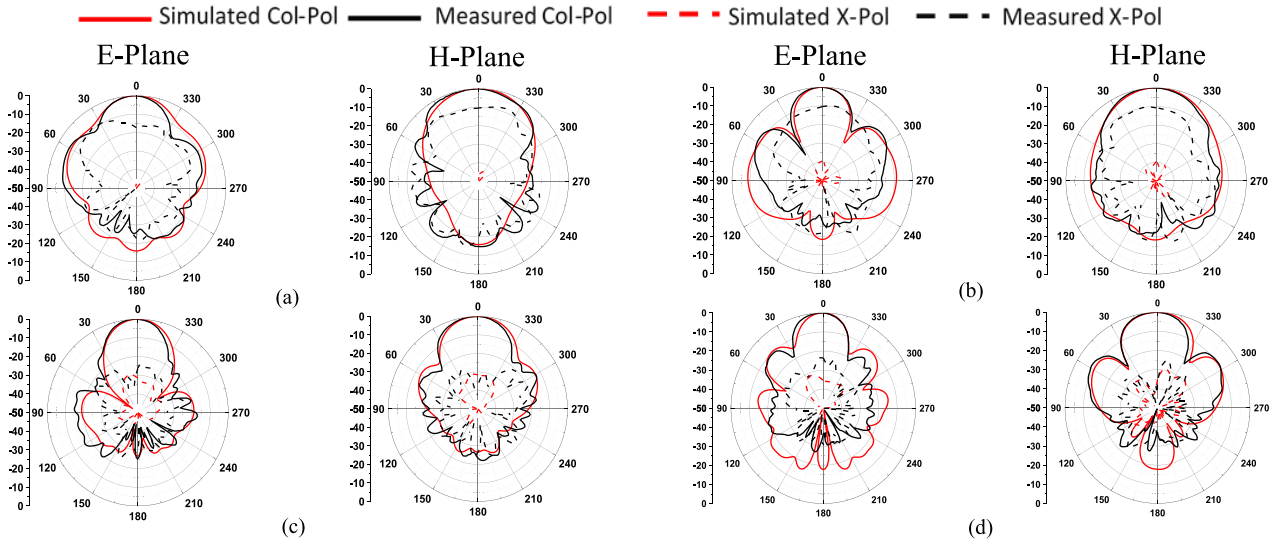

FIGURE 12. Simulated and measured radiation pattern at (a) 2.6 and (b) 3.5 GHz at the *S*-band state, at (c) 5 and (d) 6 GHz at the *C*-band state.

E. IIP$_3$

The 3rd-order intercept point at input (IIP$_3$) is characterized in measurement for several difference situations. The setup is illustrated in Fig. 14(a).

When the array operates at *C* band, all switches are forward biased. The IIP$_3$ at C band is measured to be 47.9 dBm at 6 GHz as shown in Fig. 14(b). While in the *S* band operation sate, all switches are reverse biased. It is expected that the IIP$_3$ increases against reverse bias voltage. As shown in Fig. 14(c)-(e), at $f_0 = 2.5$ GHz, IIP$_3$ is measured to be 45.2 dBm (10V), 52.6 dBm (25V) and 58.6 dBm (50V), respectively.

F. BEAM STEERING CAPABILITY

The beamsteering at both bands (3 and 5 GHz) is demonstrated. All ports are excited to realize vertical polarization. Fig. 15(a) (Fig. 15(b)) shows the beamscanning to 10° in E plane (15° in H plane) at 3 GHz. While Fig. 15(c) (Fig. 15(d)) shows the beamscanning to 15° in E plane (20° in H plane) at 5 GHz. It should be noted that several delays lines were built and used to emulate the phases as specified in Fig. 15(e) to facilitate the beamsteering pattern measurement.

In a digital array, multiple signals can be fed into one antenna port to enable independent multiple beams scanning

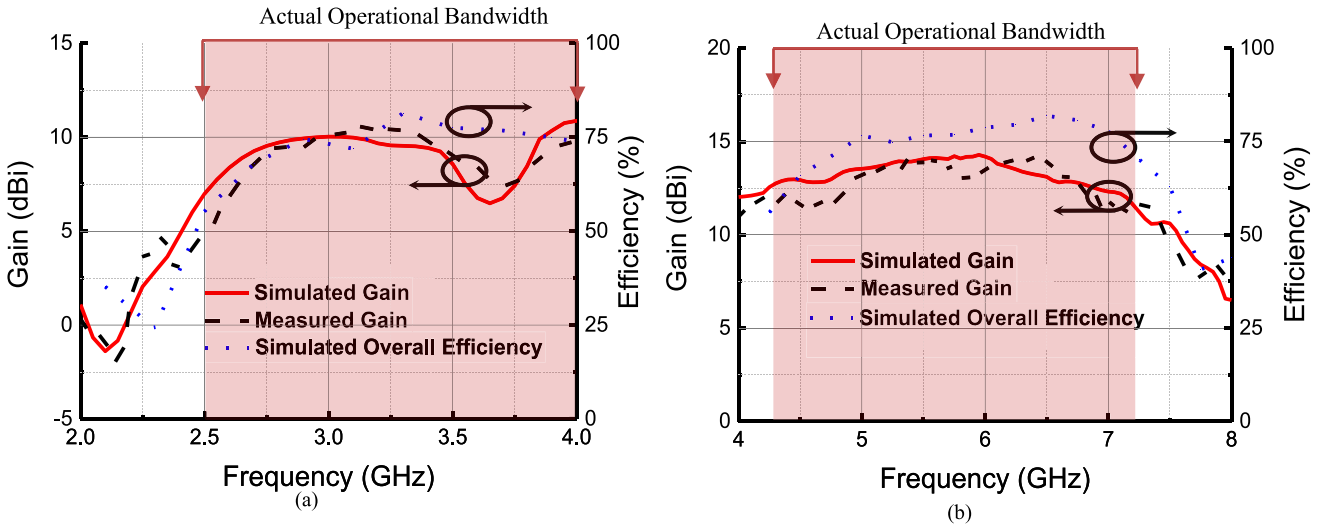

FIGURE 13. Realized gain (Simulated and measured) and overall efficiency (simulated) at the (a) *S*- and (b) *C*-band state.

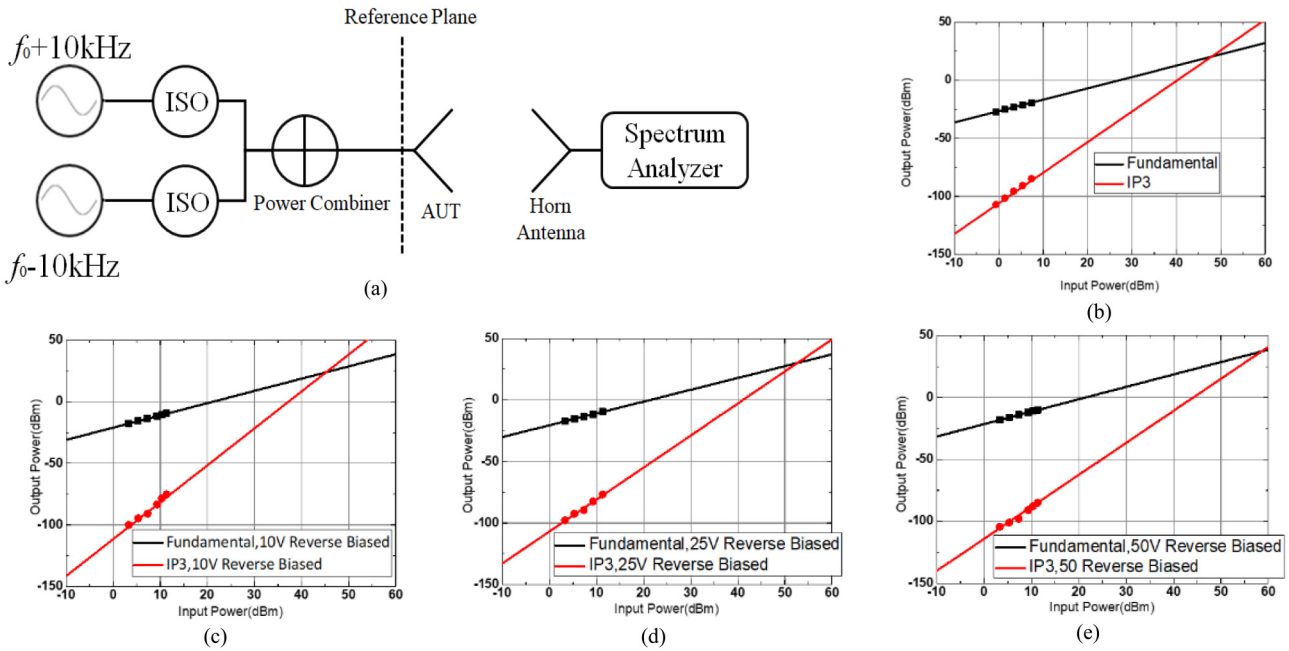

FIGURE 14. (a) IIP_3 measurement setup. (b) Measured IIP_3 in the *C*-band state (switches are forward biased) and *S*-band state with (c) 10V reverse biased, (d) 25V reverse biased, (e) 50V reverse biased. Two isolators (ISOs) are used for the *S* band (RFLI-301-4) and *C* band (RFLI-402-4). Both are from RF-LAMBDA.

at different directions. This possibility is demonstrated using HFSS simulations. In Fig. 16(a) (Fig. 16(b)), a V-pol. (H-pol.) beam scans in the horizontal (vertical) direction. Combined together, two independent aforementioned beams can be created (as shown in Fig. 16(c)) using a digital array.

The simulated active S parameters for the 2×2 *S*-band/4×4 *C*-band array with different scan angles are presented in Fig. 17. The active S parameters for the *S*-band port is below −10 dB when the beam scans in the E plane. However, in the H plane, the active S_{11} rises to −6 dB when beam scans to 35°. On the other hand, the active S parameters for the *C*-band ports remain below −10 dB at different scan angles in both E and H planes. The active S parameters at some frequency points rise to −5 dB.

G. CIRCULAR POLARIZATION CAPABILITY

This array can easily support CP for a digital array. The phases at each antenna port for right-handed CP (RHCP) operations are illustrated in Fig. 18(a). When the phases are sequentially rotated in the other direction, left-hand CP (LHCP) can be achieved. The simulated axial ratios (ARs) are below 0.2 dB at *S* band and 0.8 dB at *C* band. as shown in Fig. 18(b)-(c). The radiation patterns at

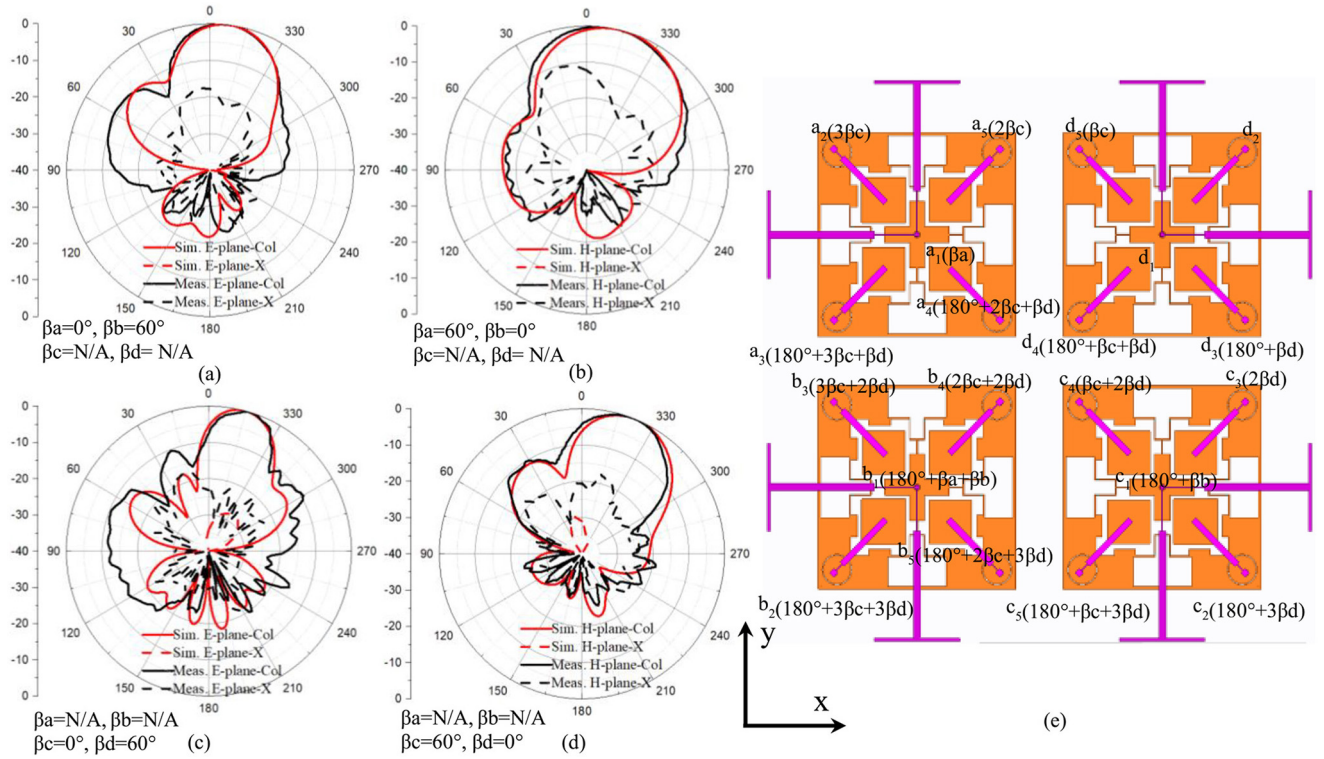

FIGURE 15. Simulated and measured radiation patterns for a 2×2 *S*-band array scanning at 3 GHz along (a) Y-axis and (b) X-axis. Simulated and measured radiation patterns for a 4×4 *C*-band array scanning at 5 GHz along (c) Y-axis and (d) X-axis. (e) Phase arrangement at each port.

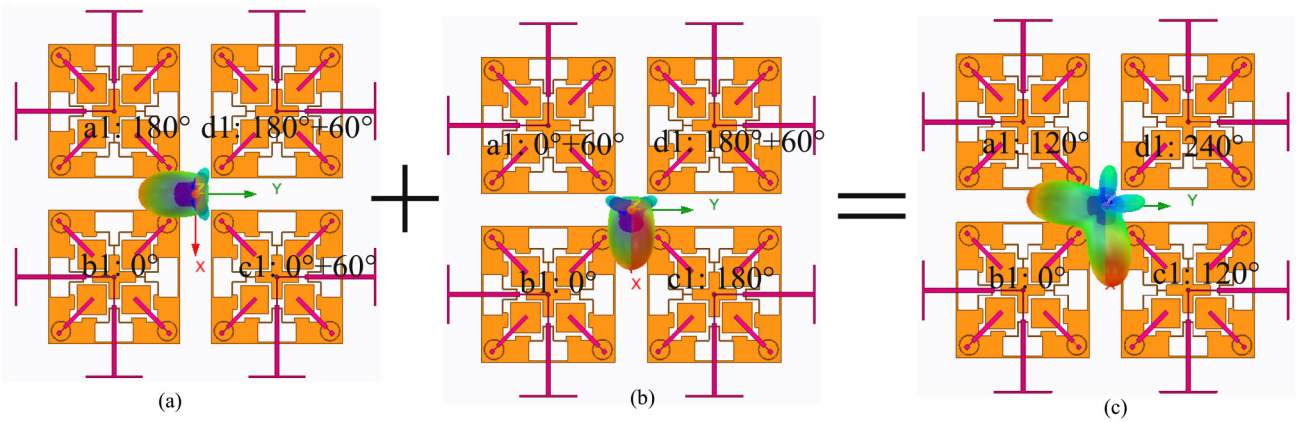

FIGURE 16. The 2×2 *S*-band array (a) polarizes along X-axis and scans along Y-axis and (b) polarizes along Y-axis and scans along X-axis at 3GHz. (c) Independent dual-beam scanning at 3 GHz.

2, 3.5, 5 and 6 GHz were simulated in HFSS and presented in Fig. 18(d)-(g).

IV. ARRAY II DESIGN

A. MOTIVATION OF IMPLEMENTING AMC

In Array I, a solid ground plane is used below the radiation aperture. The electrical distance between the radiation aperture and ground plane is $\lambda_0/4$ at 4.7 GHz. At the edges of the entire frequency range of 2-8 GHz, this $\lambda_0/4$ condition can be hardly satisfied, leading to reduced operational bandwidth.

In Array II, an AMC layer is added in between the radiation aperture and ground plane. This AMC can provide the equivalent $\lambda_0/4$ condition at 2.8 GHz and 6.6 GHz, respectively. As a result, the bandwidth, gain and overall efficiency of the antenna array can be significantly improved.

B. FRACTAL-SHAPED SLOT-RING ANTENNA APERTURE

The fractal shape design at both *S* and *C* bands is very similar to Array I. However, there are a few critical improvements in Array II. First, The *C*-band ports are moved from the outside corners to the inside corners as shown in Fig. 19(a). The benefits of this change are twofold: (1) the size of the

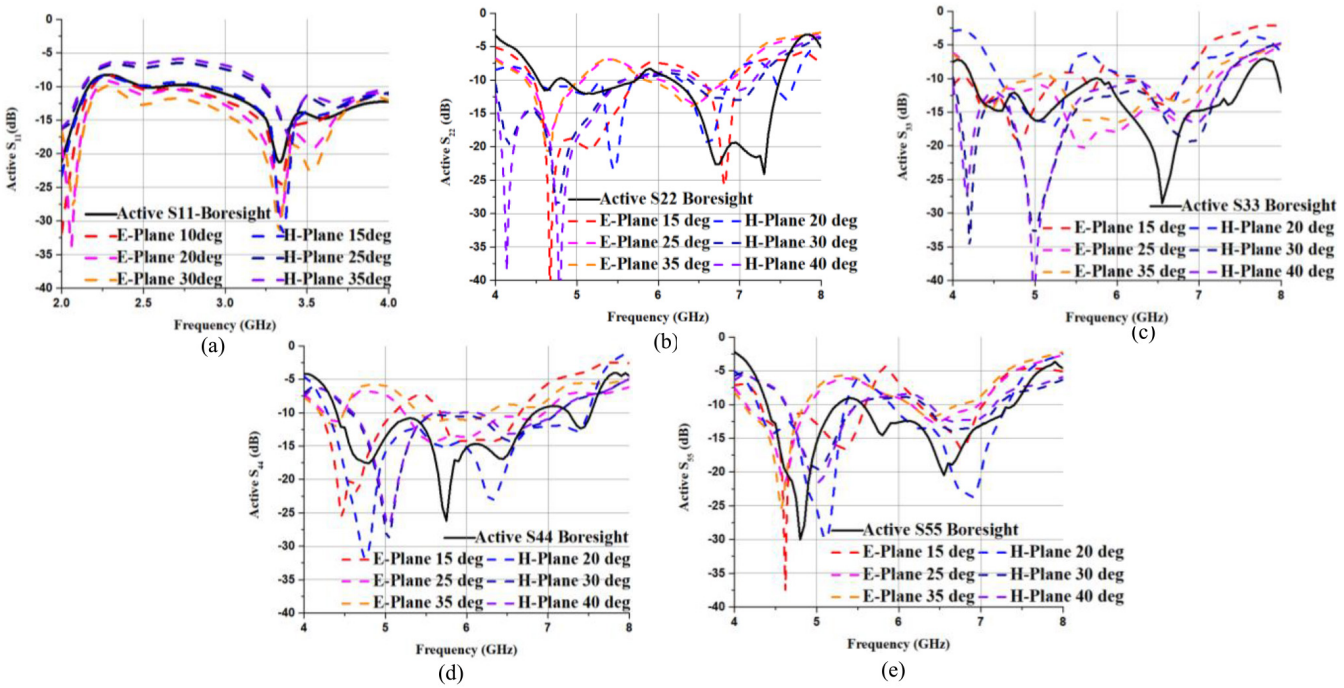

FIGURE 17. (a) Active S_{11} in the *S*-band state vs. different scan angles. Active (b) S_{22}, (c) S_{33}, (d) S_{44} and (e) S_{55} in the *C*-band state vs. different scan angles.

S-band antenna element is much smaller; (2) the unfavorable effects on the realized gain of the Array I *S*-band element are minimized since the two of the *C*-band ports are at the maximum electric field of the *S*-band antenna element (Fig. 2(a) Antenna III). Second, the *S*-band feeding lines are bent at the edge of the *S*-band element so that $\lambda/2$ spacing can be met for a modular array. Third, it was found that the four solid metal strips surrounding the *S*-band port in Array I deteriorates the gain of the *C*-band elements. Since these metal strips also act as the ground plane of the *S*-band microstrip feeding lines, A meander design is implemented in Array II to avoid the aforementioned issue while at the same time it still provides a ground for the *S*-band feeding lines. Finally, since the four *C*-band ports are much closer in Array II, four L-shaped floating metal strips (marked in yellow in Fig. 19) are used to improve the isolation among the four ports.

As shown in Fig. 19(a), eight PIN diode switches are embedded in the radiation aperture allowing the switching of operational frequency bands similar to Array I. In array II, as shown in Fig. 19(b), additional switches are embedded in both *S* and *C* band feeding lines to further improve the isolation between the two frequency bands. In Section V, it will be shown that the isolation can be improved by an additional 20(10) dB at *S*(*C*) band. To provide the DC voltage bias for all these switches, metals in the radiation aperture are segmented and shown in different colors shown in Fig. 19. The contour and feeding lines of the *S*-band element (both in purple color) are connected to V_1 through the bias wire at the right edge. A 10-kΩ resistor is used to connect the contour and feeding lines together. Approximately half of the contour of the *C*-band elements and their feeding lines (both in orange color) are connected to ground through the outer conductor of the coax lines at Ports 2-5. Again, these two pieces of metals are connected through 10-kΩ resistors. V_2 and V_3 are provided through the inner conductor of Port 1 and Ports 2-5, respectively.

C. AMC LAYER DESIGN

Periodic square loops [44] is adopted here to achieve a band-stop resonance around 10 GHz as shown in Fig. 20(a). This structure is equivalent to a transmission line loaded with a series LC resonator. The AMC layer is designed on a 31-mil-thick Rogers RT/Duroid 6002 substrate ($\varepsilon_r = 2.9$, $\tan\delta = 0.0012$) and the dimensions of the AMC structure are given in Fig. 20.

When the AMC layer is incorporated into Array II as shown in Fig 20(b). the entire structure can be modeled as the equivalent circuit in Fig. 20(b). The simulated S_{11} phase of a unit cell is equal to 0° at both 2.8 and 6.6 GHz.

V. ARRAY II FABRICATION AND MEASUREMENT

A. ANTENNA FABRICATION

The radiation aperture is fabricated on the same substrate for the AMC layer. The feeding lines, radiation aperture, and AMC are shown in Fig. 21(a)-(c). In the AMC layer, five small holes are drilled to pass the coax feeding lines while the eight square holes provide replacement access to the eight PIN diode switches. First, PIN diode switches and resistors are soldered to the radiation aperture. The five coax

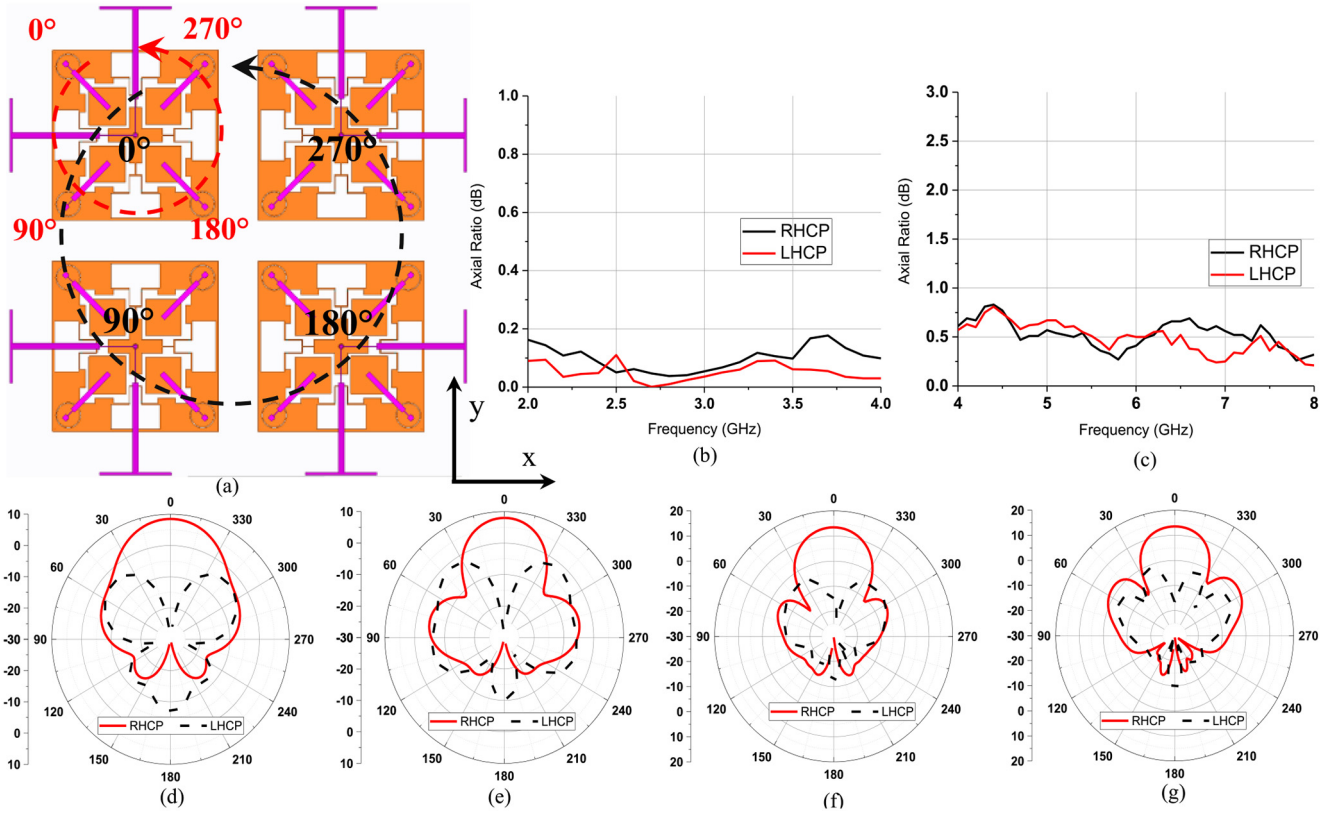

FIGURE 18. (a) Phase configuration for RHCP operation inside a 2×2 array at *S*- and *C*-band state; axial ratio for LHCP and RHCP at boresight direction at (b) *S*- and (c) *C*-band state; simulated RHCP radiation pattern along the xz plane (d) at 2.6 and (e) 3.5 GHz in the *S*-band state, (f) at 5 and (g) 6 GHz in the *C*-band state.

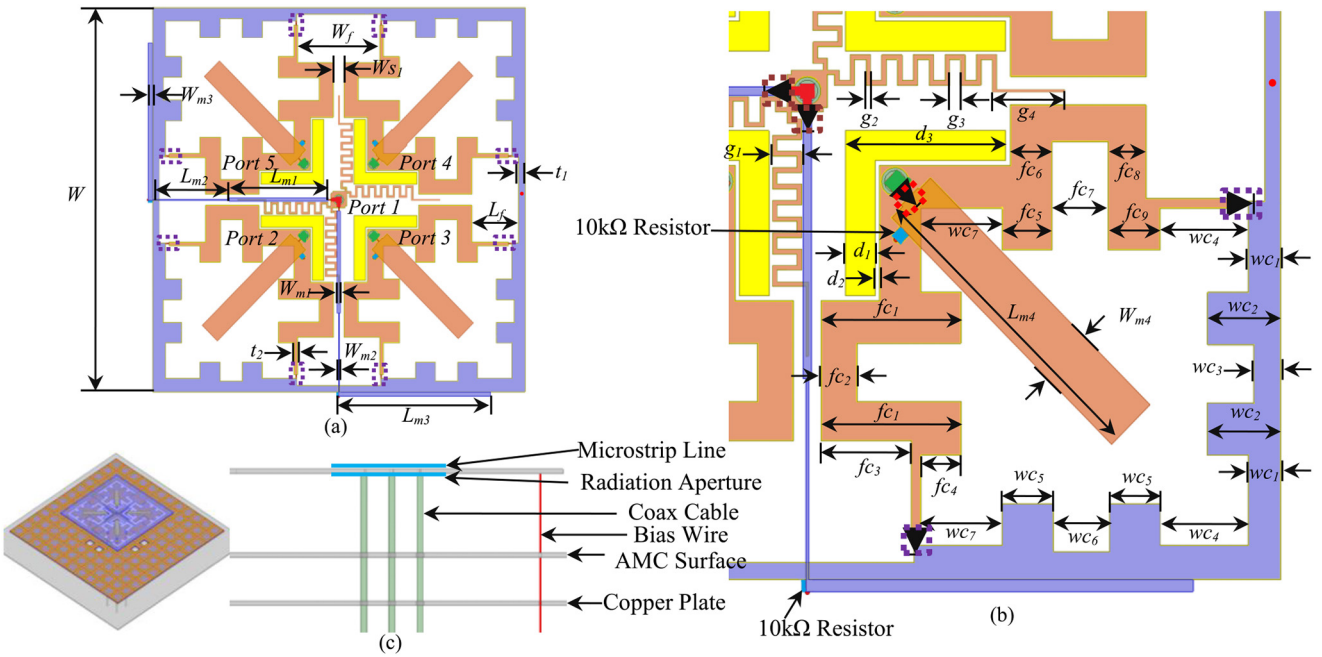

FIGURE 19. (a) Schematic of Array II. (b) Zoom-in view of one *C*-band antenna. (c) Side view. $W = 42$, $Lm_1 = 11.17$, $Lm_2 = 8.6$, $Lm_3 = 11.7$, $Lm3 = 13.76$, $Wm_1 = 0.35$, $Wm_2 = 0.1$, $Wm_3 = 0.5$, $Wm_3 = 2.42$, $L_f = 5.25$, $W_f = 9.3$, $t_1 = 0.73$, $t_2 = 0.42$, $Ws_1 = 1.2$, $g_1 = 1.3$,$g_2 = 0.2$, $g_3 = 0.5$, $g_3 = 3.2$, $d_1 = 1.3$, $d_2 = 0.2$, $d_3 = 7.1$, $fc_1 = 6.23$, $fc_2 = 1.6$, $fc_3 = 4.0$, $fc_4 = 1.8$, $fc_5 = 2.2$, $fc_6 = 1.85$, $fc_7 = 2.5$, $fc_8 = 1.66$, $fc_9 = 2.3$, $wc_1 = 1.47$, $wc_2 = 3.26$, $wc_3 = 1.2$, $wc_4 = 3.89$, $wc_5 = 2.25$, $wc_6 = 2.5$, $wc_7 = 3.6$. (All dimensions are in mm.)

lines then assembled and soldered to the radiation aperture. Finally, the copper plate is assembled to the antenna. In this design, we did not use the double-layer ground plane in Array II. Instead, large holes are drilled in the ground plane and then sealed using copper tapes (Fig. 21(e). The assembled Array II is shown in Fig. 21(d).

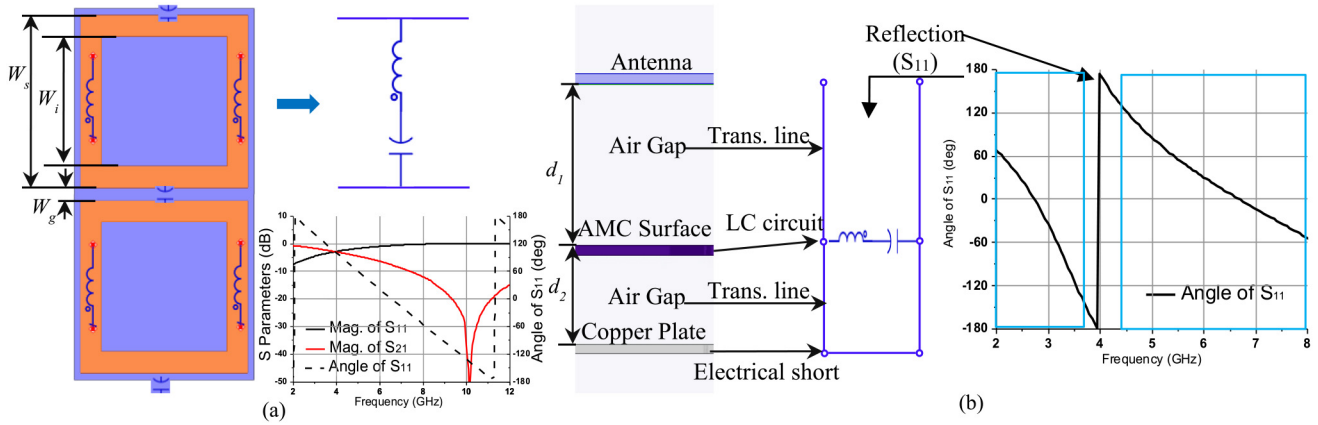

FIGURE 20. (a) AMC unit cell, equivalent circuit and S parameters. (b) AMC in Array II, equivalent circuit and S_{11} phase. $W_g = 0.72$, $W_s = 6.78$, $W_i = 5.08$, $d_1 = 13$, $d_2 = 8$. (All dimensions are in mm.)

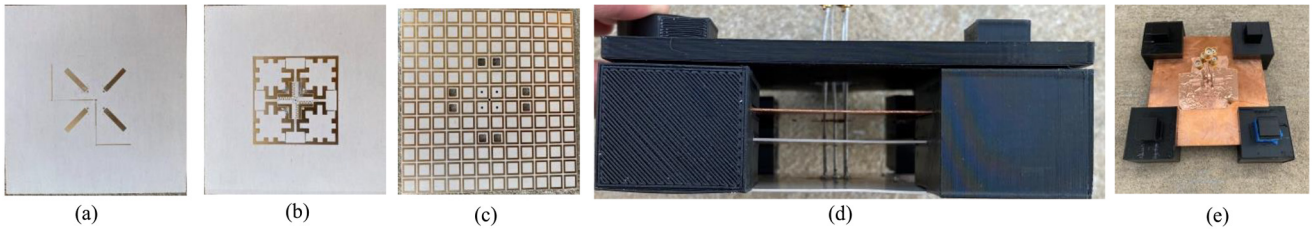

FIGURE 21. (a) Top and (b) bottom side of the radiation aperture. (c) AMC surface. (d) Side and (e) bottom view of the entire antenna assembly.

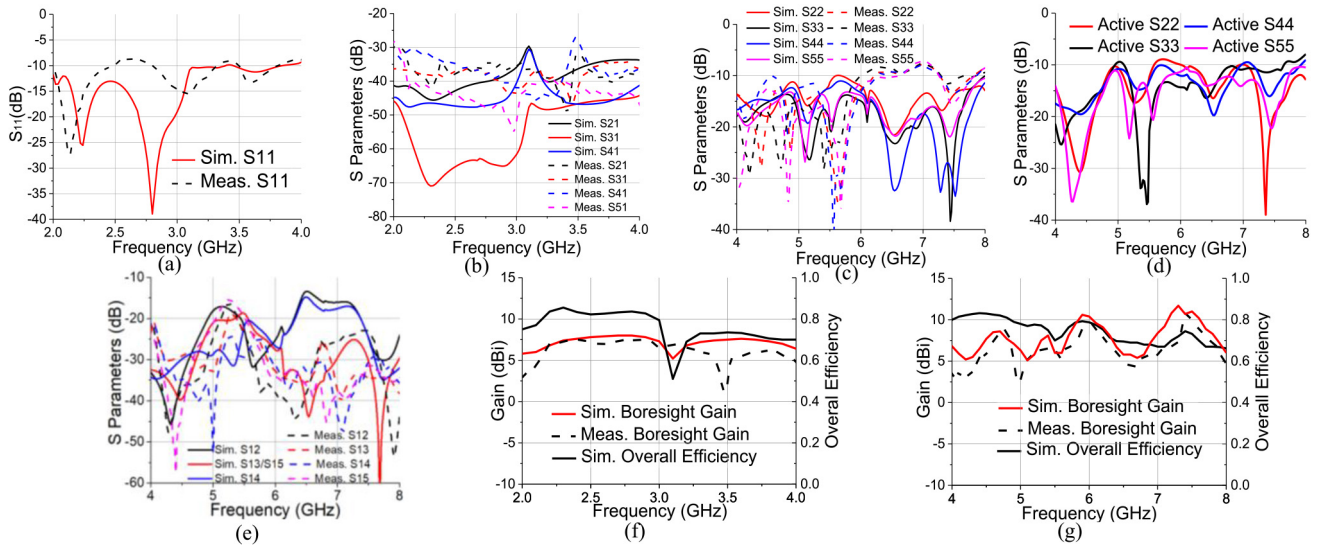

FIGURE 22. Simulated and measured (a) S_{11}, (b) $S_{21}/S_{31}/S_{41}/S_{51}$ at *S*-band state. (c) Simulated and measured $S_{22}/S_{33}/S_{44}/S_{55}$ at *C*-band state. (d) Active $S_{22}/S_{33}/S_{44}/S_{55}$ at *C*-band state., (e) Simulated and measured $S_{12}/S_{13}/S_{14}/S_{15}$ at *C*-band state. Simulated and measured realized gain at boresight for (f) *S*- and (g) *C*-band state.

B. MEASUREMENT RESULTS

In *S*-band operation state, the simulated and measured S_{11} satisfies the -10dB criteria in most of the frequency range of 2-4 GHz (Fig. 22(a)). The measured isolation between the *S* band port and the four *C*-band ports is better than 30 dB at most of the frequency range (Fig. 22(b)), compared to 10 dB in Array I. In *C*-band operation state, the simulated and measured reflection coefficients are below −10 dB in most of the frequency range of 4-8 GHz (Fig. 22(c)). The simulated active S parameters for *C*-band ports (Fig. 22(d)) are very close to the reflection coefficients. The measured isolation between the *C*-band ports and *S*-band port is better than 20 dB at most of the frequency range of 4-8 GHz (Fig. 22(e)), compared to 10 dB in Array I. It is noted that when Array II operates in *S*(*C*) band, the PIN diodes in the *C*(*S*) band feeding lines are turned off. The improvement in

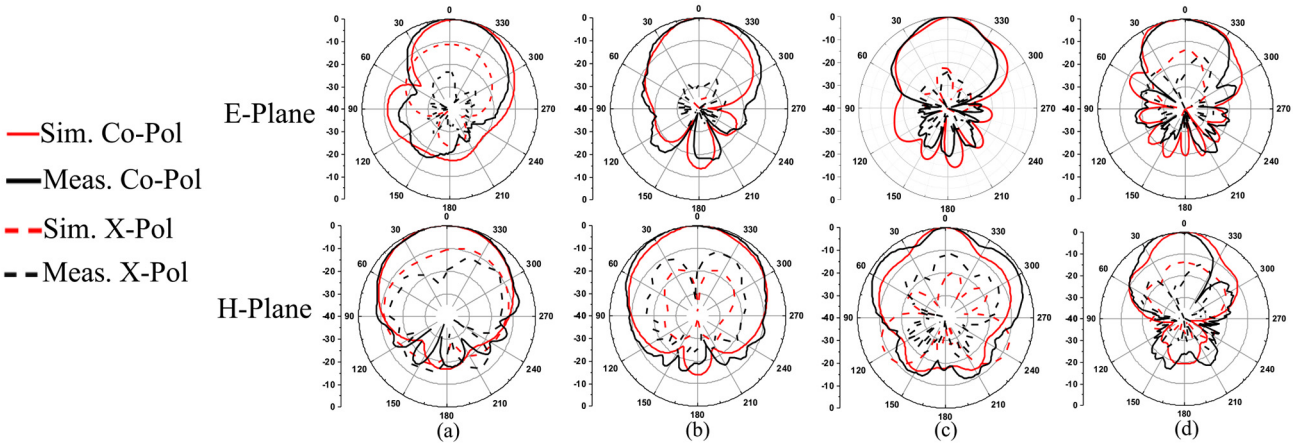

FIGURE 23. Simulated and measured radiation patterns at (a) 2.2 and (b) 3.8 GHz in *S*-band state; and at (c) 4.8 and (d) 7.0 GHz in *C*-band state.

TABLE 1. Comparison of wideband or reconfigurable antenna arrays.

	Frequency Reconfigurability	Antenna Type	Operation Frequency (GHz)	Instantaneous Bandwidth	IIP_3 (dBm)	Polarization	Ports Isolation between Orthogonal Ports within Each Element	Number of ports per element
[3]	No	Patch	2.1-6.0	96.3%	N/A	Single-Pol.	None	1
[4]	Switchable	Dipole	1-2/2-4	66.7%/66.7%	N/A	Single-Pol.	None	1
[5]	No	Dipole	6-18	100%	N/A	Dual-Pol.	18dB	2
[8]	No	Vivaldi	3.8-8.6	77.5%	N/A	Dual-Pol.	20dB	2
[16]	Switchable	Dipole	3.2-4.0/4.4-5.7	21.7%/25.0%	N/A	Dual-Pol.	17dB	2
[21]	No	Slot-Ring	3-12	120%	N/A	Dual-Pol.	18dB	2
[22]	Tunable	Slot-Ring	0.9-1.6	1%	-5-30	Dual-Pol.	16dB	2
[24]	Switchable	Slot-Ring	1.8-3.5/4.4-8.8	64.2%/66.7%	>53	Dual-Pol.	4dB	2
[26]	No	Slot-Ring	2.25-2.58	13.7%	N/A	Dual-Pol.	None	1
Array I	Switchable	Slot-Ring	2.5-4/4.2-7.2	44.3%/52.6%	>45	Dual-Pol.	None	1
Array II	Switchable	Slot-Ring	2-4/4-8	66.7%/66.7%	N/A	Dual-Pol.	None	1

the isolation shown here is critical since both cases represent losses in the radiation aperture.

The simulated realized gain is 5-8 dBi at *S* band as shown in Fig. 22(f) while the measured realized gain closely matches the simulation except for a dip around 3.5 GHz, which is due to the widened radiation pattern around 3.5 GHz instead of loss. The overall efficiency at *S* band is above 68% in most of the frequency range, except for 3.1-3.2 GHz (still above 50%). The simulated realized gain is 5-12 dBi at *C* band in Fig. 22(g). The measured gain agrees well with the simulation. The simulated overall efficiency at *C* band is from 67 to 83%.

The radiation patterns are measured at 2.2 and 3.8 GHz at *S* band and 4.8 and 7.0 GHz at *C* band and shown in Fig. 23. The overall agreement between simulation and measurement is apparent. The measured X-pol. levels are much better at *S* band and similar at *C* band compared to Array I. It is noted here the ground plane in Array II is significantly larger than the *S* band antenna element.

VI. COMPARISON WITH STATE OF THE ART

Arrays I and II are compared with other wideband fixed frequency or reconfigurable antenna arrays in Table 1. The antenna arrays in [3], [4] exhibit one port at each antenna element and therefore can achieve only one polarization state. The antenna arrays in [5], [8], [16], [21], [22], [24] have two ports per element, one for each polarization state. The isolation between the two ports is compared in Table 1. It should be noted that the radiation pattern and frequency bandwidth and form factor for these arrays are very different, therefore the isolation performance needs to be carefully considered in this table. The array in [26] can reconfigure its radiation patterns and polarization in a specific way but is not suitable to be extend to a large array, potentially.

The array in [24] achieves a 4:1 frequency ration using a band-switchable approach. This arrangement can maintain $\lambda/2$ spacing at two frequency bands without the need of over-populated T/R modules. The port isolation, however, is its major weakness. The Array I (II) presented herein fundamentally solves this issue while almost maintain (maintain) the wide bandwidth performance. The radiation efficiency and realized gain are significantly improved compared to [24].

VII. CONCLUSION

A novel arraying technique has been demonstrated for polarization-reconfigurable array applications. Each array element has one feeding port only. All three polarization

states can be dynamically reconfigured by providing proper phases at each antenna port.

This new arraying technique is demonstrated inside two reconfigurable wideband (4:1 frequency ratio) arrays since wide-band multifunctional antenna arrays are the future. The band-switchable approach alleviates the need to of ultra-wideband T/R modules and over-population by providing near $\lambda/2$ spacing at each band. Therefore, high-performance single-band T/R modules can be used in Arrays I and II.

Array I is simpler in structure with one ground plane but suffers from the reduced efficiency and gain, particularly at the far ends of the operation frequency range. The performance of Array II is improved by incorporating an AMC layer. In addition, Array II is optimized in size for the design of modular arrays and enhanced in isolation performance.

REFERENCES

[1] W. Zou, S. Qu, and S. Yang, "Wideband wide-scanning phased array in triangular lattice with electromagnetic bandgap structures," *IEEE Antennas Wireless Propag. Lett.*, vol. 18, no. 3, pp. 422–426, Mar. 2019.

[2] J. Ahn, S. H. Cha, S. G. Cha, and Y. J. Yoon, "Compact spiral element for wideband beam-steering arrays," *IEEE Antennas Wireless Propag. Lett.*, vol. 16, pp. 1994–1997, 2017.

[3] Q. Liu, Z. N. Chen, Y. Liu, and C. Li, "Compact ultrawideband circularly polarized weakly coupled patch array antenna," *IEEE Trans. Antennas Propag.*, vol. 65, no. 4, pp. 2129–2134, Apr. 2017.

[4] F. Sun, F. Zhang, H. Zhang, H. Zhang, C. Li, and C. Feng, "A frequency diversity printed-Yagi antenna element for apertures selectivity wideband array application," *IEEE Trans. Antennas Propag.*, vol. 66, no. 10, pp. 5634–5638, Oct. 2018.

[5] S. Xiao, S. Yang, H. Zhang, Q. Xiao, Y. Chen, and S. Qu, "Practical implementation of wideband and wide-scanning cylindrically conformal phased array," *IEEE Trans. Antennas Propag.*, vol. 67, no. 8, pp. 5729–5733, Aug. 2019.

[6] J.-B. Yan, S. Gogineni, B. Camps-Raga, and J. Brozena, "A dual-polarized 2–18-GHz Vivaldi array for airborne radar measurements of snow," *IEEE Trans. Antennas Propag.*, vol. 64, no. 2, pp. 781–785, Feb. 2016.

[7] H. Zhang, S. Yang, Y. Chen, J. Guo, and Z. Nie, "Wideband dual-polarized linear array of tightly coupled elements," *IEEE Trans. Antennas Propag.*, vol. 66, no. 1, pp. 476–480, Jan. 2018.

[8] Y. Pan, Y. Cheng, and Y. Dong, "Dual-polarized directive ultrawideband antenna integrated with horn and Vivaldi array," *IEEE Antennas Wireless Propag. Lett.*, vol. 20, no. 1, pp. 48–52, Jan. 2021.

[9] Y. Cheng, X. Ding, W. Shao, and B. Wang, "Dual-band wide-angle scanning phased array composed of SIW-cavity backed elements," *IEEE Trans. Antennas Propag.*, vol. 66, no. 5, pp. 2678–2683, May 2018.

[10] S. Liu *et al.*, "A dual-band shared aperture antenna array in Ku/Ka-bands for beam scanning applications," *IEEE Access*, vol. 7, pp. 78794–78802, 2019.

[11] G. Kwon, J. Park, D. Kim, and K. C. Hwang, "Optimization of a shared-aperture dual-band transmitting/receiving array antenna for radar applications," *IEEE Trans. Antennas Propag.*, vol. 65, no. 12, pp. 7038–7051, Dec. 2017.

[12] J. F. Zhang, Y. J. Cheng, Y. R. Ding, and C. X. Bai, "A dual-band shared-aperture antenna with large frequency ratio, high aperture reuse efficiency, and high channel isolation," *IEEE Trans. Antennas Propag.*, vol. 67, no. 2, pp. 853–860, Feb. 2019.

[13] X. Zhang, D. Xue, L. Ye, Y. Pan, and Y. Zhang, "Compact dual-band dual-polarized interleaved two-beam array with stable radiation pattern based on filtering elements," *IEEE Trans. Antennas Propag.*, vol. 65, no. 9, pp. 4566–4575, Sep. 2017.

[14] F. Jia, S. Liao, and Q. Xue, "A dual-band dual-polarized antenna array arrangement and its application for base station antennas," *IEEE Antennas Wireless Propag. Lett.*, vol. 19, no. 6, pp. 972–976, Jun. 2020.

[15] S.-S. Zhong, Z. Sun, L.-B. Kong, C. Gao, W. Wang, and M.-P. Jin, "Tri-band dual-polarization shared-aperture microstrip array for SAR applications," *IEEE Trans. Antennas Propag.*, vol. 60, no. 9, pp. 4157–4165, Sep. 2012.

[16] Z. Nie, H. Zhai, L. Liu, J. Li, D. Hu, and J. Shi, "A dual-polarized frequency-reconfigurable low-profile antenna with harmonic suppression for 5G application," *IEEE Antennas Wireless Propag. Lett.*, vol. 18, no. 6, pp. 1228–1232, Jun. 2019.

[17] H. Li, L. Kang, F. Wei, Y. Cai, and Y. Yin, "A low-profile dual-polarized microstrip antenna array for dual-mode OAM applications," *IEEE Antennas Wireless Propag. Lett.*, vol. 16, pp. 3022–3025, 2017.

[18] Y. Gao, R. Ma, Y. Wang, Q. Zhang, and C. Parini, "Stacked patch antenna with dual-polarization and low mutual coupling for massive MIMO," *IEEE Trans. Antennas Propag.*, vol. 64, no. 10, pp. 4544–4549, Oct. 2016.

[19] X. Jiang, Z. Zhang, Y. Li, and Z. Feng, "A planar wideband dual-polarized array for active antenna system," *IEEE Antennas Wireless Propag. Lett.*, vol. 13, pp. 544–547, 2014.

[20] C. Lee, S. Chen and P. Hsu, "Isosceles triangular slot antenna for broadband dual polarization applications," *IEEE Trans. Antennas Propag.*, vol. 57, no. 10, pp. 3347–3351, Oct. 2009.

[21] R. V. S. R. Krishna and R. Kumar, "A dual-polarized square-ring slot antenna for UWB, imaging, and radar applications," *IEEE Antennas Wireless Propag. Lett.*, vol. 15, pp. 195–198, 2016.

[22] C. R. White and G. M. Rebeiz, "Single- and dual-polarized tunable slot-ring antennas," *IEEE Trans. Antennas Propag.*, vol. 57, no. 1, pp. 19–26, Jan. 2009.

[23] M. Shirazi, T. Li, J. Huang, and X. Gong, "A reconfigurable dual-polarization slot-ring antenna element with wide bandwidth for array applications," *IEEE Trans. Antennas Propag.*, vol. 66, no. 11, pp. 5943–5954, Nov. 2018.

[24] M. Shirazi, J. Huang, T. Li, and X. Gong, "A switchable S-/C-Band antenna array with dual polarization and modularity," *IEEE Trans. Antennas Propag.*, vol. 68, no. 2, pp. 783–794, Feb. 2020.

[25] L. A. Greda and A. Dreher, "Tx-terminal phased array for satellite communication at Ka-band," in *Proc. Eur. Microw. Conf.*, 2007, pp. 266–269, doi: 10.1109/EUMC.2007.4405177.

[26] J. Row and Y. Huang, "Reconfigurable antenna with switchable broadside and conical beams and switchable linear polarized patterns," *IEEE Trans. Antennas Propag.*, vol. 66, no. 7, pp. 3752–3756, Jul. 2018, doi: 10.1109/TAP.2018.2820325.

[27] J. Huang, "Switchable slot-ring antennas for customizable phased array applications," Ph.D. dissertation, Dept. Electr. Comput. Eng., Univ. Central Florida, Orlando, FL, USA, 2021. [Online]. Available: https://stars.library.ucf.edu/etd2020/700

[28] D. N. Elsheakh, H. A. Elsadek, E. A. Abdallah, H. Elhenawy, and M. F. Iskander, "Enhancement of microstrip monopole antenna bandwidth by using EBG structures," *IEEE Antennas Wireless Propag. Lett.*, vol. 8, pp. 959–962, 2009, doi: 10.1109/LAWP.2009.2030375.

[29] S.-H. Kim, J.-Y. Lee, T. T. Nguyen, and J.-H. Jang, "High-performance MIMO antenna with 1-D EBG ground structures for handset application," *IEEE Antennas Wireless Propag. Lett.*, vol. 12, pp. 1468–1471, 2013, doi: 10.1109/LAWP.2013.2288797.

[30] S. Kim, Y. Ren, H. Lee, A. Rida, S. Nikolaou, and M. M. Tentzeris, "Monopole antenna with inkjet-printed EBG array on paper substrate for wearable applications," *IEEE Antennas Wireless Propag. Lett.*, vol. 11, pp. 663–666, 2012, doi: 10.1109/LAWP.2012.2203291.

[31] B. S. Abirami and E. F. Sundarsingh, "EBG-backed flexible printed Yagi–Uda antenna for on-body communication," *IEEE Trans. Antennas Propag.*, vol. 65, no. 7, pp. 3762–3765, Jul. 2017, doi: 10.1109/TAP.2017.2705224.

[32] M. S. Khan, F. A. Tahir, A. Meredov, A. Shamim, and H. M. Cheema, "A W-band EBG-backed double-rhomboid bowtie-slot on-chip antenna," *IEEE Antennas Wireless Propag. Lett.*, vol. 18, no. 5, pp. 1046–1050, May 2019, doi: 10.1109/LAWP.2019.2908891.

[33] L. Yousefi, B. Mohajer-Iravani, and O. M. Ramahi, "Enhanced bandwidth artificial magnetic ground plane for low-profile antennas," *IEEE Antennas Wireless Propag. Lett.*, vol. 6, pp. 289–292, 2007, doi: 10.1109/LAWP.2007.895282.

[34] M. Li, Q. L. Li, B. Wang, C. F. Zhou, and S. W. Cheung, "A low-profile dual-polarized dipole antenna using wideband AMC reflector," *IEEE Trans. Antennas Propag.*, vol. 66, no. 5, pp. 2610–2615, May 2018, doi: 10.1109/TAP.2018.2806424.

[35] J. D. D. Ntawangaheza, L. Sun, C. Yang, Y. Pang, and G. Rushingabigwi, "Thin-profile wideband and high-gain microstrip patch antenna on a modified AMC," *IEEE Antennas Wireless Propag. Lett.*, vol. 18, no. 12, pp. 2518–2522, Dec. 2019, doi: 10.1109/LAWP.2019.2942056.
[36] J. Lin, Z. Qian, W. Cao, S. Shi, Q. Wang, and W. Zhong, "A low-profile dual-band dual-mode and dual-polarized antenna based on AMC," *IEEE Antennas Wireless Propag. Lett.*, vol. 16, pp. 2473–2476, 2017, doi: 10.1109/LAWP.2017.2724540.
[37] S. Sarkar and B. Gupta, "A dual-band circularly polarized antenna with a dual-band AMC reflector for RFID readers," *IEEE Antennas Wireless Propag. Lett.*, vol. 19, no. 5, pp. 796–800, May 2020, doi: 10.1109/LAWP.2020.2980325.
[38] Q. Liu, H. Liu, W. He, and S. He, "A low-profile dual-band dual-polarized antenna with an AMC reflector for 5G communications," *IEEE Access*, vol. 8, pp. 24072–24080, 2020, doi: 10.1109/ACCESS.2020.2970473.
[39] H. Zhai, K. Zhang, S. Yang, and D. Feng, "A low-profile dual-band dual-polarized antenna with an AMC surface for WLAN applications," *IEEE Antennas Wireless Propag. Lett.*, vol. 16, pp. 2692–2695, 2017, doi: 10.1109/LAWP.2017.2741465.
[40] J. Huang and X. Gong, "A wide-band dual-polarized frequency-reconfigurable slot-ring antenna element using a diagonal feeding method for array design," in *Proc. IEEE APS/URSI*, Boston, MA, USA, 2018, pp. 477–478.
[41] W. Chen, G. Wang, and C. Zhang, "Bandwidth enhancement of a microstrip-line-fed printed wide-slot antenna with a fractal-shaped slot," *IEEE Trans. Antennas Propag.*, vol. 57, no. 7, pp. 2176–2179, Jul. 2009.
[42] C. Borja and J. Romeu, "On the behavior of Koch Island fractal boundary microstrip patch antenna," *IEEE Trans. Antennas Propag.*, vol. 51, no. 6, pp. 1281–1291, Jun. 2003.
[43] M. Shirazi, J. Huang, T. Li, and X. Gong, "A Switchable-frequency slot-ring antenna element for designing a reconfigurable array," *IEEE Antennas Wireless Propag. Lett.*, vol. 17, no. 2, pp. 229–233, Feb. 2018, doi: 10.1109/LAWP.2017.2781463.
[44] B. A. Munk, *Frequency Selective Surfaces: Theory and Design*. New York, NY, USA: Wiley, 2000.

J. HUANG (Member, IEEE) received the B.S. degree in electrical engineering from the Beijing University of Posts and Telecommunications, Beijing, China, in 2010, the M.S. degree in electrical engineering from the New Jersey Institute of Technology, Newark, NJ, USA, in 2012, and the Ph.D. degree in electrical engineering from the University of Central Florida, Orlando, FL, USA.

From 2012 to 2015, he was with the Aviation Industry Corporation of China, Shanghai, China. He is also a Research Assistant with the Antenna, RF and Microwave Integrated Systems Laboratory, University of Central Florida from 2015 to 2021. He is currently a Senior BAW Filter Designer with Qorvo, Apopka, FL, USA. His research interests include phased array antennas, reconfigurable antenna arrays, and passive microwave components.

Dr. Huang was awarded to be the Finalist in 2018 and the Honorable Mention Award in 2019 and 2020 of the IEEE AP Symposium Student Paper Competition. He was the Vice Chair of the IEEE AP/MTT Orlando Chapter from 2019 to 2021. He has served as a Reviewer for the IEEE AP-S/URSI *International Symposium on Antennas and Propagation*. He is a member of the IEEE Antennas and Propagation (AP) Society and the Microwave Theory and Techniques (MTT) Society.

M. SHIRAZI (Member, IEEE) received the Ph.D. degree in electrical engineering from the University of Central Florida, Orlando, FL, USA, in 2018.

He is currently a Senior Antenna Engineer with Qualcomm Inc., San Diego, CA, USA. His current research interests include phased array antennas, reconfigurable antenna arrays, antennas for 5G and Internet of Things, microwave components, filters, and sensors.

Dr. Shirazi received the Best Student Research Presentation Award from the 2017 IEEE Wireless and Microwave Technology Conference and the Honorable Mention Award of the Student Paper Competition from the 2016 IEEE International Workshop on Antenna Technology. He was the Chair of the IEEE AP/MTT Orlando Chapter in 2018. He has served as a Reviewer for the IET Microwaves, Antennas and Propagation, and the 2018 and 2019 IEEE AP-S/URSI International Symposium on Antennas and Propagation. He is a member of the IEEE Antennas and Propagation Society and the Microwave Theory and Techniques Society.

X. GONG (Senior Member, IEEE) received the B.S. and M.S. degrees in electrical engineering from Fudan University, Shanghai, China, in 1997 and 2000, respectively, and the Ph.D. degree in electrical engineering from the University of Michigan, Ann Arbor, MI, USA, in 2005.

He joined the University of Central Florida (UCF), Orlando, FL, USA, as an Assistant Professor, in 2005. He was a Postdoctoral Research Associate with the Birck Nanotechnology Center, Purdue University, West Lafayette, IN, USA, in 2005. He was with the Air Force Research Laboratory, Hanscom, MA, USA, in 2009, under the support of the Air Force Office of Scientific Research Summer Faculty Fellowship Program. He is currently a Professor of electrical and computer engineering with UCF, where he is also the Director of the Antenna, RF and Microwave Integrated Systems Laboratory. His current research interests include microwave passive components and filters, sensors, antennas and arrays, flexible electronics, and packaging.

Dr. Gong was a recipient of the NSF Faculty Early CAREER Award in 2009, the Teaching Incentive Program Award from UCF in 2010 and 2015, and the UCF Lockheed Martin Professorship from 2018 to 2023. He received the Outstanding Engineer Awards from the IEEE Florida Council and Orlando Section in 2009, the UCF Reach for the Stars Award in 2016, and the Research Incentive Award from UCF in 2011, 2016, and 2021. He was the Chair of the IEEE AP/MTT Orlando Chapter from 2007 to 2010. He was the Technical Program Committee Chair of the 2013 IEEE AP-S/URSI International Symposium on Antennas and Propagation, the Operations Chair of the 2014 IEEE MTT-S International Microwave Symposium, and the General Chair of the 2016 IEEE International Workshop on Antenna Technology and the 2012 IEEE Wireless and Microwave Technology Conference. He has served on the Editorial Board of the IEEE TRANSACTIONS ON MICROWAVE THEORY AND TECHNIQUES, the IEEE TRANSACTIONS ON ANTENNAS AND PROPAGATION, the IEEE MICROWAVE AND WIRELESS COMPONENTS LETTERS, and the IEEE ANTENNAS AND WIRELESS PROPAGATION LETTERS. He served as an Associate Editor for the IEEE MICROWAVE AND WIRELESS COMPONENTS LETTERS from 2013 to 2018. He was an Associate Editor of the IEEE TRANSACTIONS ON MICROWAVE THEORY AND TECHNIQUES from 2018 to 2019.